Physics in Medicine & Biology

IPEM Institute of Physics and Engineering in Medicine

NOTE • **OPEN ACCESS**

Characterization and evaluation of a flexible MRI receive coil array for radiation therapy MR treatment planning using highly decoupled RF circuits

To cite this article: Kiaran P McGee *et al* 2018 *Phys. Med. Biol.* **63** 08NT02

IOP Publishing Phys. Med. Biol. **63** (2018) 08NT02 (14pp) https://doi.org/10.1088/1361-6560/aab691

Physics in Medicine & Biology

IPEM Institute of Physics and Engineering in Medicine

RECEIVED
2 June 2017

REVISED
28 February 2018

ACCEPTED FOR PUBLICATION
14 March 2018

PUBLISHED
13 April 2018

NOTE

Characterization and evaluation of a flexible MRI receive coil array for radiation therapy MR treatment planning using highly decoupled RF circuits

Kiaran P McGee[1], **Robert S Stormont**[2], **Scott A Lindsay**[2], **Victor Taracila**[2], **Dennis Savitskij**[2], **Fraser Robb**[2], **Robert J Witte**[1], **Timothy J Kaufmann**[1], **John Huston III**[1], **Stephen J Riederer**[1], **Eric A Borisch**[1] and **Phillip J Rossman**[1]

[1] Department of Radiology, Mayo Clinic and Foundation, Rochester, MN, United States of America
[2] GE Healthcare, Waukesha, WI, United States of America

E-mail: mcgee.kiaran@mayo.edu

Keywords: magnetic resonance imaging, radiofrequency, radiation therapy treatment planning

Abstract

The growth in the use of magnetic resonance imaging (MRI) data for radiation therapy (RT) treatment planning has been facilitated by scanner hardware and software advances that have enabled RT patients to be imaged in treatment position while providing morphologic and functional assessment of tumor volumes and surrounding normal tissues. Despite these advances, manufacturers have been slow to develop radiofrequency (RF) coils that closely follow the contour of a RT patient undergoing MR imaging. Instead, relatively large form surface coil arrays have been adapted from diagnostic imaging. These arrays can be challenging to place on, and in general do not conform to the patient's body habitus, resulting in sub optimal image quality. The purpose of this study is to report on the characterization of a new flexible and highly decoupled RF coil for use in MR imaging of RT patients. Coil performance was evaluated by performing signal-to-noise ratio (SNR) and noise correlation measurements using two coil (SNR) and four coil (noise correlation) element combinations as a function of coil overlap distance and comparing these values to those obtained using conventional coil elements. *In vivo* testing was performed in both normal volunteers and patients using a four and 16 element RF coil. Phantom experiments demonstrate the highly decoupled nature of the new coil elements when compared to conventional RF coils, while *in vivo* testing demonstrate that these coils can be integrated into extremely flexible and form fitting substrates that follow the exact contour of the patient. The new coil design addresses limitations imposed by traditional surface coil arrays and have the potential to significantly impact MR imaging for both diagnostic and RT applications.

1. Introduction

In modern MR scanners signal reception is achieved by using either transmit-receive or receive-only radiofrequency (RF) coils. While local transmit-receive coils such as a birdcage design head coil provide uniform RF fields within their volume and therefore spatially uniform MR images (Haacke *et al* 1999), they are limited in their application due to their fixed geometry. Multi-channel (element) receive-only RF coils address many of the limitations of local transmit-receive coils by disassociating transmit and receive functions. RF transmission is performed by a separate large volume or whole body birdcage coil while reception is performed using a 2D array of individual coil elements encased within a semi-rigid housing.

In its most basic form a single channel RF coil as used for magnetic resonance imaging (MRI) signal reception consists of a conductive loop of copper fabricated onto a nonconductive fiberglass substrate that is sectioned by high quality or high '*Q*' factor capacitors. The circuit is completed by the addition of an impedance-matched resonant circuit that allows tuning of the resonant frequency of the circuit to the Larmor frequency of the MR

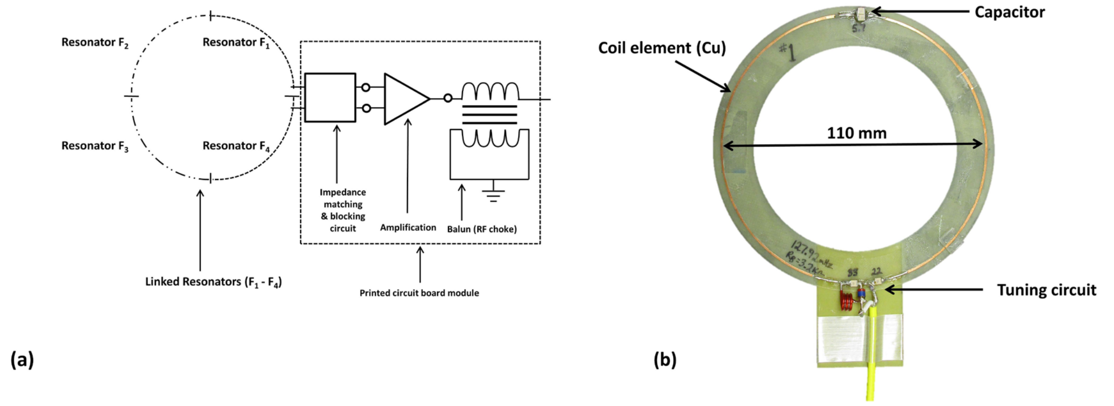

Figure 1. Single element RF coil designs for AIR (a) and conventional copper (b) loops. The AIR coil consists of linked resonator elements connected to a printed circuit board module (dashed lines). The conventional copper based coil element consists of a thin copper loop and high Q-value capacitor etched onto a thin fiberglass base. The circuit is tuned to the resonant frequency of protons at a field strength of 3.0 T (127.9 MHz) by means of the tuning circuit shown.

scanner (Fujita 2007). The detected MR signal is in the form of an electromotive force that is induced in the loop in accordance with Faraday's law of induction. The signal is then amplified and digitized.

Multichannel RF coils consist of multiple single coil elements that have been designed to provide uniform signal reception, with a smooth and predictable falloff as a function of distance from the coil surface across the dimensions of the composite coil. To achieve this, considerable effort is dedicated to the size and placement of individual coils as well as the amount of overlap between adjacent coils. Coil size and placement impact signal uniformity, particularly as a function of depth while coil overlap affects coupling between adjacent coil elements due to mutual inductance (Roemer *et al* 1990). This effect is minimized when the amount of overlap is some fraction of the coil dimension. For circular coils, the optimal theoretical overlap is equal to 0.25× the diameter of the coil (Roemer *et al* 1990). Due to these considerations, modern receive-only RF coils are relatively constrained both in terms of their design and rigidity, despite the development of so-called flexible surface coil arrays. The inclusion of tuning and blocking circuits close to each coil element further adds to their physical bulk, weight, and rigidity (Fujita 2007).

In 2017, a new flexible and low physical profile RF coil element design referred to as adaptive image receive (AIR) coil was described and characterized (Rossman *et al* 2017). The RF coil possesses unique electrical properties in which the effects of mutual inductance and capacitive coupling between coil elements are significantly reduced thereby allowing coils to be placed with higher coil density in configurations that could not be achieved using conventional RF coils. In addition, their high flexibility and low physical profile allows them to be integrated into materials such as blankets or sheets that can conform directly to individual patient contours, especially when the patient is placed into a desired radiation therapy (RT) treatment position. These new coil designs therefore hold the promise of addressing many of the limitations that conventional surface coil arrays have placed on the MR imaging of patients for RT treatment planning and simulation.

The purpose of this work was to characterize the performance of these new AIR coils by comparing them to conventional, copper based RF coil elements. Phantom studies were performed to compare the SNR of both coil types and to compare SNR maps as a function of coil overlap distance for two element coil combinations. Mutual inductance loop to loop coupling was quantified by calculating noise correlation matrices for four element coil combinations. Parallel imaging performance was assessed by calculating *g*-factor maps as a function of coil overlap distance. *In vivo* testing was performed using four and 16-element coils in both normal volunteers and a patient undergoing MR imaging for RT treatment planning of the cervical spine.

2. Methods

All imaging was performed on two 3 T MR scanners with bore diameters of 60 cm (Signa HDx, GE Healthcare, Waukesha WI) and 70 cm (750W, GE Healthcare, Waukesha WI). Data analysis was performed using an in-house software application (MRView, Mayo Clinic and Foundation).

2.1. Multichannel RF coils description

All multichannel AIR coils were constructed using multiple identical single loop coils. The diameter of each coil element was equal to 110 mm and consisted of a malleable conductor with an approximate diameter of 0.6 mm resulting in a flexible low profile form factor loop that can conform precisely to complex and irregular surface contours. Figure 1(a) is a schematic of the AIR coil design that includes the resonant loop consisting of four

Table 1. Imaging parameters for phantom and *in vivo* imaging experiments described in this work. SE = spin echo, GE = gradient echo, MESE = multi echo spin echo, TE = echo time, TR = pulse repetition time, TI—inversion time, FLAIR = fluid attenuated inversion recovery.

Experiment Number	FOV (mm)	Mode	Freq. × Phase × loc.	TE/TR (msec)	Signal averages	TI (msec)	Slice thickness (mm)	Echo Type	Echo train length	Flip angle (degrees)	Bandwidth (kHz)
1	400	2D	256 × 224	9/150	1	—	5	SE	—		31.3
2	220	3D	256 × 96 × 38	1.6/3.444	1	—	3	GE		5	125
3	220	2D	320 × 224	9/2500	1	920	5	SE FLAIR	7	—	62.4
3	220	2D	256 × 256	100.5/3000	2	—	5	MESE	12	—	50
4	240	3D	256 × 256 × 108	74/2002	1	—	1.2	MESE	50	—	166.6
5	280	3D	288 × 288 × 128	23/602	2	—	1.4	MESE	24	—	166.6

linked resonators. For a given coil, the number of resonators is determined by its circumference (as in the case of a circular loop).The loop is created from a flexible link resonator structure using a process that is proprietary to the MR scanner manufacturer (GE Healthcare, Waukesha, WI) with the length of each resonator being no greater than 1/10th of the wavelength of the resonant RF field (Veenstra and Long 2008). This ensures that the resonator does not behave as a transmission line but rather a lumped element circuit thereby ensuring a uniform charge distribution and internally confined irrotational electric fields within the resonator (Sutherland 1999). The ensemble of resonators creates a zero reactance, low loss and low interaction loop that can be modeled electrically as a lumped circuit but without any physical lumped components providing high flexibility and durability. The resonant loop is connected to a printed circuit board module (dashed box in figure 1(a)) of dimensions 26.5 mm × 26.5 mm × 10 mm. The module provides impedance matching, signal amplification, and an RF choke and replaces conventional coil circuitry including the preamplifier, decoupler, matching circuit, and baluns. The preamplifier is low noise and is tolerant of a wide range of loop loading conditions. The combination of the conductor and electronics module provides a complete imaging coil element which exhibits lowered interaction to adjacent elements, extreme flexibility, and high performance. A single triaxial cable is used to connect the coil loop to the MR scanner so as to receive the MR signal. While a fixed diameter of 110 mm was used for all coil elements in this work, any diameter loop can be fabricated and constructed.

For the purposes of comparison a second multichannel RF coil set was constructed using conventional copper based coil elements of equal diameter as shown in figure 1(b). Individual elements consisted of a single 110 mm diameter copper loop and a pair of high Q capacitors as shown. The coil element was tuned to the resonant frequency of 127.92 MHz using a network analyzer (Agilent Technologies Japan, Hyogo, Japan). Multichannel coils were created by combining multiple elements of the single loop design.

2.2. Coil characterization

2.2.1. Signal-to-noise ratio (SNR) performance

A series of experiments was performed to evaluate the SNR of a single and double loop AIR coil configuration and to compare these values to those obtained from equal diameter conventional RF coil(s). For the double coil, both coil types included overlaps of 0 mm, 24 mm, 30 mm and 50 mm, with the 24 mm overlap being the nominal overlap distance for 110 mm diameter coils. This value is slightly less than the value of 27.5 mm estimated by Roemer *et al* (1990) and was obtained by minimizing the mutual inductance experimentally using a network analyzer (Agilent Technologies Japan, Hyogo, Japan).

All SNR measurements were conducted by placing the RF coils on top of a non-loading rectangular phantom (Dielectric Corporation, USA) of dimensions 380 mm × 155 mm × 155 mm filled with a dimethyl silicone–gadolinium solution. The phantom and coil combinations were imaged on the aforementioned 60 cm bore diameter 3 T MR scanner using a T_1-weighted spin echo pulse sequence whose parameters are listed in table 1 under the row denoted Experiment Number 1. A 2D imaging plane bisecting the middle of the coil element(s) and orthogonal to the plane of the coil was prescribed. For each acquisition, an SNR image was calculated according to the National Electrical Manufacturers Association (NEMA) standard MR 9-2008 (National Electrical Manufacturers Association (NEMA) 2008) by dividing the entire image by the standard deviation of a region of interest of 25 × 25 pixels in the background (i.e. air) region of the image. The SNR maps were then normalized by dividing the SNR images by the maximum SNR value from the AIR and conventional coil data.

For the paired coil SNR maps, a sub region equal to a width of 385 mm and length of 80 mm with the width being parallel to the coil surface and length being perpendicular was chosen. Histograms of the normalized SNR values were calculated over the range of 0–1.0 with bin widths equal to 0.1. For each histogram the mean and standard deviation of the distribution were calculated. For SNR values within the region of interest, a one way analysis of variance and Tukey's range test were performed for each coil type and overlap distance using the OriginPro 9 data analysis and graphing package (OriginLab Corporation, Northhampton, MA USA).

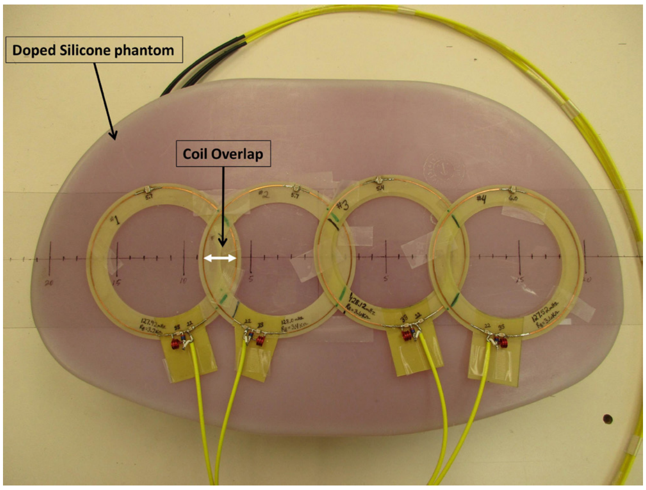

Figure 2. Four element phased array coil with each coil element arranged linearly. The coil elements are placed on top of a non electrically loading doped silicone phantom. The configuration allows the overlap between adjacent coil elements to be varied.

2.2.2. *Assessment of noise correlation*

To estimate the amount of correlated noise between various coil elements, and by inference the amount of mutual inductance between them, a noise correlation matrix was calculated using the method described by Ohliger and Sodickson (2006). Noise correlation matrices were calculated for four channel multichannel coil combinations using both AIR and conventional coils. Both coil sets were assembled in a linear array and were placed on a torso shaped non electrically loading phantom (Dielectric Corporation, Milwaukee, WI) whose widest dimensions were 450 mm × 260 mm × 100 mm and filled with a dimethyl silicone–gadolinium solution as shown in figure 2. For each coil set five separate experiments at coil overlaps of 0 mm, 10 mm, 25 mm, 40 mm and 50 mm were performed. Data were obtained using the methodology described (Kellman and McVeigh 2005) in which the noise within each RF channel was sampled in the absence of RF and spatial encoding gradient fields using an ultra-fast 3D spoiled gradient echo imaging sequence whose parameters are listed in table 1 as Experiment Number 2. All imaging was performed on the previously described 60 cm bore diameter 3 T MR scanner.

2.2.3. *Assessment of parallel imaging performance*

Assessment of parallel imaging performance was determined by calculating so-called *g*-factor maps according to the methodology described by Pruessmann *et al* (1999). These maps were derived from the data acquired to estimate noise correlation matrices previously described. The *g*-factor maps utilize the full noise correlation matrices, with the noise sample data acquisition integrated into the scan pre-excitation.

2.3. *In vivo* testing

2.3.1. *Evaluation of coil flexibility*

To demonstrate the flexible and form fitting nature of the AIR coils, four coil elements were sewn around the sides and posterior of a Lycra® balaclava. No elements were placed anteriorly due to the opening for the face. There was no preference given for overlaps between adjacent coil elements and the overlaps were equal to 5 mm (coils 3 & 4), 12 mm (coils 1 & 2) and 20 mm (coils 2 & 3). The balaclava design provided a flexible and exact form fitting coil design free of any rigid housings used in conventional coils. The coil combination was then placed on the head and neck of a male volunteer as shown in figure 3. Axial T_1 FLAIR and T_2 multi echo spin echo images were acquired on the aforementioned 3 T 60 cm MR scanner using the parameters listed in table 1 as described in Experiment Number 3. All imaging was performed under an Institutional Review Board approved research protocol with written informed consent being obtained prior to imaging.

2.3.2. *RT planning coil*

To assess the performance of the multichannel AIR coils for the purpose of MR imaging of patients undergoing RT treatment planning, a sixteen channel RF coil was constructed by combining individual AIR coil elements. Coils were grouped into four, four-channel paddles. For each paddle, the four coils were placed in a clover leaf configuration as shown in figure 4 with an overlap of 30 mm between adjacent coil elements and no overlap between any of the four elements at the center of the array configuration. The coils and resonant modules were sandwiched between two 3 mm thick sheets of polyester backed neoprene rubber (Foam Order Factory, San Pablo, CA) of dimensions 215 mm × 280 mm.

[redacted] [redacted] [redacted]

Figure 3. Balaclava with four AIR coil elements placed on a normal volunteer.

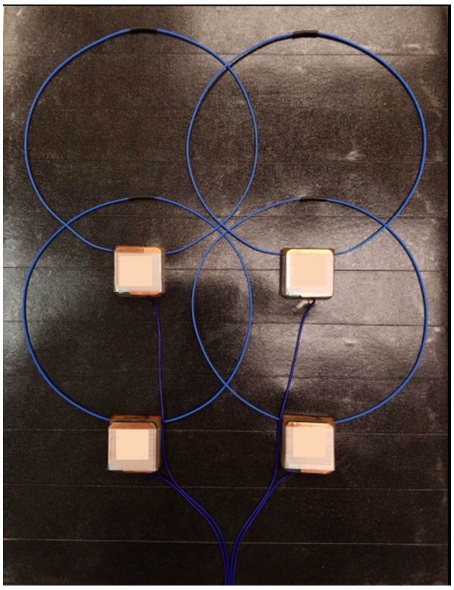

Figure 4. Four AIR coil elements arranged in a clover leaf pattern. The four coil configuration represents one paddle of the four paddles of the 16-element RF coil designed for *in vivo* testing in normal volunteers and patients undergoing MR imaging for RT treatment planning.

A normal female volunteer and male patient undergoing MR imaging for RT treatment planning were imaged using the 16 channel AIR coil and a manufacturer provided combination 30 channel US Food and Drug Administration (FDA) approved RF coil set designed for RT treatment planning (RT Suite, GE Healthcare, Waukesha, WI). The FDA approved coil configuration consisted of a four coil combination that provided a total 30 individual coil elements and included a posterior array consisting of 8 coil elements encased within a rigid housing, two 3-element flex coils designed to be placed around the head and a 16 element rectangular flexible array coil. All imaging was performed under an Institutional Review Board approved research protocol with written informed consent being obtained prior to imaging. For both individuals two identical image data sets were obtained; the first with the FDA approved RT treatment planning RF coils and the second with the 16-channel AIR RF coil array. All imaging was performed on a 70 cm 3 T MR scanner previously described. Table 1 lists the scan parameters used to acquire the 3D data sets for the volunteer and treatment planning data and are listed as Experiment Number 4 and 5 respectively. For both data sets parallel imaging using the technique known as autocalibrating reconstruction for cartesian sampling (ARC) (Brau *et al* 2008) was used with acceleration factor of 2 in both

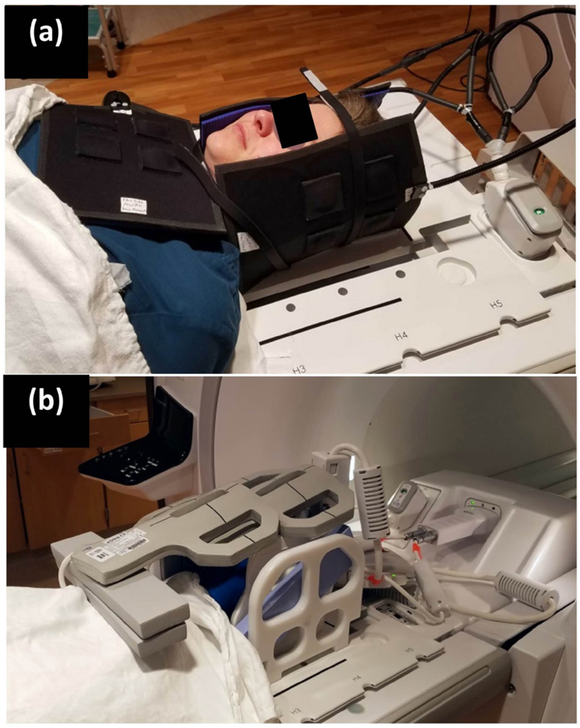

Figure 5. Placement of 16 element AIR coil and 30 element FDA approved RT Suite coils on a normal volunteer. (a) 16 channel AIR coil placement. The coil consists of 4 black paddles with each paddle containing 4 coil elements. (b) 30 element RT suite coil combination.

phase and slab encoding directions resulting in a total acceleration factor of 4. For the volunteer study a sagittal T_2-weighted non fat saturated acquisition was acquired while a sagittal T_1-weighted 3 point iterative Dixon-based fat saturation (Skinner and Glover 1997, Reeder *et al* 2004) acquisition was used for the patient study.

The cervical spines of both the volunteer and RT patient were imaged using the two coil configurations shown in figures 5(a) and (b). Both subjects were first positioned on top of a MR compatible indexed flat table top insert (CIVCO Radiotherapy, Orange City, IA, USA). For the AIR coil combination (figure 5(a)) a single four element paddle was placed below the cervical spine. Two four element paddles where placed against the left and right side of the subject's head while the final four element paddle was placed on the anterior chest at the level of the clavicles. Individual paddles were held in place using thin Velcro straps. Figure 5(b) shows the configuration used when imaging with the RT Suite and involved placing the two 3 element coils directly on top of the face of the subject, the 16 element flexible coil around the sides of the patient's head with the 8 element posterior array inserted into the table of the MR scanner below the flat table insert.

3. Results

3.1. Phantom testing

Figure 6 shows SNR plots as a function of perpendicular distance from the coil surface for the single coil (figure 6(a)) and 24 mm overlap double coil (figure 6(b)) configurations for both coil types respectively. For the single coil the profile was taken at the center of the coil while for the double coil comparison profiles were taken at the middle of the overlap between the two coils. In the single coil comparison (figure 6(a)) The AIR coils provided improved SNR compared to the conventional coil up to a depth of approximately 25 mm. For the two coil comparison (figure 6(b)), the conventional coil SNR was 12% higher at the surface of the coil. However, at distances beyond one millimeter from the surface of the coil both coils exhibited similar SNR values as a function of depth.

Figure 7 shows the SNR maps for the two element coil configuration as a function of overlap distance for both the conventional and AIR coils. The gray scale image at the top of the figure shows a representative magnitude image from which the SNR maps were derived. The yellow dashed line shows the region from which the eight SNR maps were obtained. All maps have been normalized to the maximum SNR value obtained from all data which was equal to the AIR coil SNR map at an overlap of zero millimeters. Coil overlap is identified by the red 'H' symbol above each map. Inductive coupling between adjacent coil elements due non-ideal coil overlap is seen in the non-uniformity of the coil SNR maps, particularly close to the surface of the coil. The conventional coil maps exhibit greater non-uniformity compared to the AIR coils. At the optimal overlap distance of 24 mm,

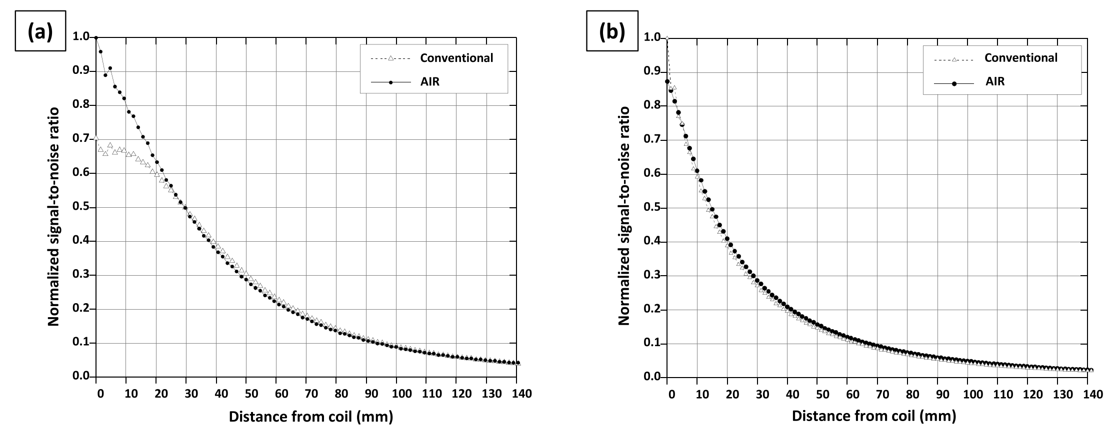

Figure 6. Signal-to-noise ratio (SNR) as a function of perpendicular distance from the RF coil surface for a single coil (a) and double coil configuration (b). For the single coil, the profile was located at the center of the coil. For the double coil configuration, the profile was taken along a line normal to the midpoint between coil centers. A value of 1.0 represents the global SNR maximum for all coil combinations and types.

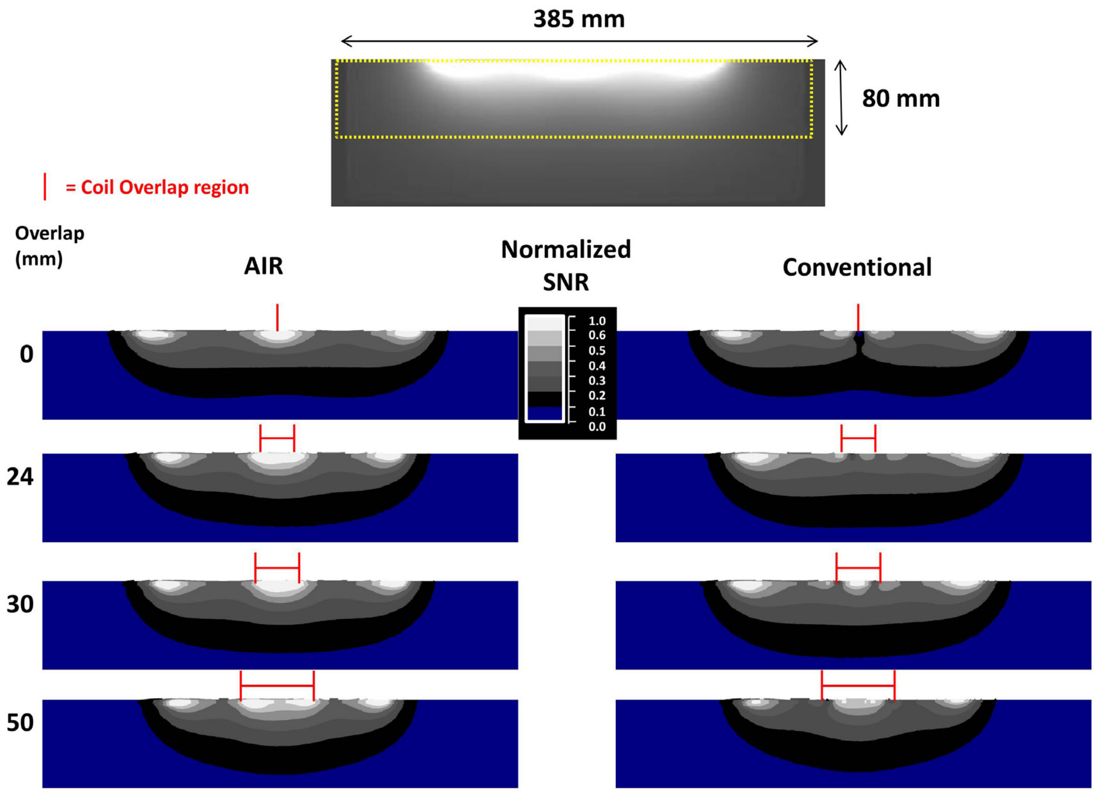

Figure 7. Normalized signal-to-noise ratio (SNR) plots as a function of coil overlap for a two element RF coil. The top image shows the original image used to calculate SNR values with the dashed box representing the zoomed region shown in the figures below. The SNR maps as a function of overlap distance were normalized to the maximum SNR obtained from all eight SNR maps. Coil overlap is identified by the red 'H' symbol above each SNR map.

both coil types exhibit similar SNR maps. However, at distances of 0 mm and 30 mm the AIR coil SNR maps are visually closer to the 24 mm overlap map compared to the conventional coils. At a maximum overlap of 50 mm, the SNR maps of the two coil types are approximately equivalent, demonstrating that at some distance, both coils will suffer from degraded SNR due to mutual inductance between adjacent coil elements. Of note, the SNR plots shown in the figure have been quantized into 7 individual bins with equal bin sizes of 0.1 from 0 to 0.6. The final bin size is equal to 0.4 and includes the SNR range from 0.6 to 1.0.

Table 2 lists the mean and standard deviation of the histogram of SNR values when binned in 0.1 increments starting at a value of 0.0 while table 3 lists the results of performing Tukey's range test for two coil combinations of conventional and AIR coils versus coil overlap distance. For each comparison an alpha value (significance level) of 0.05 was used. In table 3 the first column lists the coil comparison being tested where C and A denote the

Table 2. Normalized SNR for conventional and AIR coils as a function of overlap.

Coil	Overlap (mm)	Histogram mean	Histogram standard deviation
Conventional	0	0.123 14	0.1116
	24	0.130 29	0.1244
	30	0.129 63	0.1262
	50	0.101 51	0.1075
AIR	0	0.131 62	0.1252
	24	0.128 21	0.1335
	30	0.126 74	0.1346
	50	0.117 34	0.1328

Table 3. Tukey's range test of normalized signal-to-noise ratio (SNR) data for two coil combinations of conventional and AIR coils versus coil overlap distance. For each comparison an alpha value (significance level) of 0.05 was used. C = conventional coil, A = AIR coil, LCL = lower confidence limit, UCL = upper confidence limit, q = studentized range statistic. A significance value of 1 indicates that the means are statistically significant. For all tests the standard error of the mean was equal to 0.001 57.

Comparison	Mean difference	q value	Probability	Significance	LCL	UCL
C_24: C_0	0.007 16	6.4341	1.4521×10^{-4}	1	0.002 39	0.011 92
C_30: C_0	0.006 49	5.836 12	$9.606 77 \times 10^{-4}$	1	0.001 72	0.011 26
C_30: C_24	$-6.650 79 \times 10^{-4}$	0.597 98	0.999 89	0	−0.005 43	0.0041
C_50: C_0	−0.021 63	19.446 63	$3.330 67 \times 10^{-16}$	1	−0.0264	−0.016 86
C_50: C_24	−0.028 78	25.880 73	$3.330 67 \times 10^{-16}$	1	−0.033 55	−0.024 02
C_50: C_30	−0.028 12	25.282 75	$3.330 67 \times 10^{-16}$	1	−0.032 89	−0.023 35
A_0: C_0	0.008 48	7.624 71	$1.941 07 \times 10^{-6}$	1	0.003 71	0.013 25
A_0: C_24	0.001 32	1.190 61	0.990 69	0	−0.003 44	0.006 09
A_0: C_30	0.001 99	1.788 59	0.911 81	0	−0.002 78	0.006 76
A_0: C_50	0.030 11	27.071 34	$3.330 67 \times 10^{-16}$	1	0.025 34	0.034 88
A_24: C_0	0.005 07	4.562 72	0.0275	1	$3.074 27 \times 10^{-4}$	0.009 84
A_24: C_24	−0.002 08	1.871 38	0.8903	0	−0.006 85	0.002 69
A_24: C_30	−0.001 42	1.2734	0.986 11	0	−0.006 18	0.003 35
A_24: C_50	0.0267	24.009 35	$3.330 67 \times 10^{-16}$	1	0.021 94	0.031 47
A_24: A_0	−0.003 41	3.061 99	0.373 08	0	−0.008 17	0.001 36
A_30: C_0	0.0036	3.237 57	0.299 35	0	−0.001 17	0.008 37
A_30: C_24	−0.003 56	3.196 53	0.315 83	0	−0.008 32	0.001 21
A_30: C_30	−0.002 89	2.598 55	0.594 28	0	−0.007 66	0.001 88
A_30: C_50	0.025 23	22.6842	$3.330 67 \times 10^{-16}$	1	0.020 46	0.03
A_30: A_0	−0.004 88	4.387 14	0.040 44	1	−0.009 65	$-1.121 43 \times 10^{-4}$
A_30: A_24	−0.001 47	1.325 15	0.982 47	0	−0.006 24	0.003 29
A_50: C_0	−0.0058	5.213 23	0.005 58	1	−0.010 57	−0.001 03
A_50: C_24	−0.012 95	11.647 34	$5.329 07 \times 10^{-15}$	1	−0.017 72	−0.008 19
A_50: C_30	−0.012 29	11.049 36	$1.565 41 \times 10^{-13}$	1	−0.017 06	−0.007 52
A_50: C_50	0.015 83	14.2334	$3.330 67 \times 10^{-16}$	1	0.011 06	0.0206
A_50: A_0	−0.014 28	12.837 94	$3.330 67 \times 10^{-16}$	1	−0.019 05	−0.009 51
A_50: A_24	−0.010 87	9.775 95	$1.331 58 \times 10^{-10}$	1	−0.015 64	−0.006 11
A_50: A_30	−0.0094	8.450 81	$6.402 31 \times 10^{-8}$	1	−0.014 17	−0.004 63

conventional and AIR coils respectively. The numerical value denotes the overlap distance. For example, A_24: C_30 tests the SNR values of the AIR coil with an overlap of 24 mm compared to the conventional coil combination at an overlap of 30 mm. The second column describes the difference in means of the two SNR distributions. A positive difference denotes that the first coil combination's mean was greater than the second coil combination. A negative value denotes the opposite. The results of this statistical test are also shown in figure 8 for the various coil combinations as a function of overlap distance. Statistically significant differences in means between various coil combinations are shown in red while non-significant differences in means are shown in black. A total of six combinations had mean differences greater than 0.02. The difference in mean SNR values for the coil at an overlap of 50 mm and conventional coil at overlaps of 0 mm, 24 mm and 30 mm were negative and greater than 0.02 indicating that the 50 mm overlap distance provided the lowest SNR compared to the others and that these differences were statistically significant. For positive differences greater than 0.02 the AIR coil mean at overlap

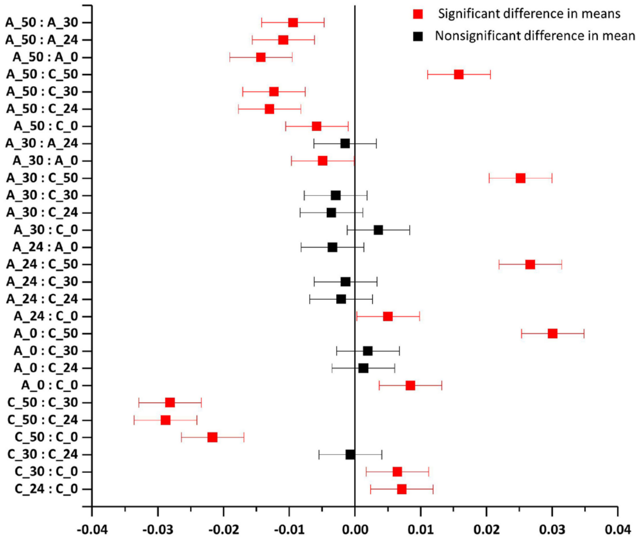

Figure 8. Statistical comparison of normalized signal-to-noise ratio (SNR) means as a function of coil type and overlap for two coil combinations using the Tukey test for analysis of variance. The ordinate axis lists the coil comparisons where the alpha numeric code identifies the coil type (C = conventional, A = AIR) and overlap distance in millimeters. Mean differences that are red are statistically significant while black are not.

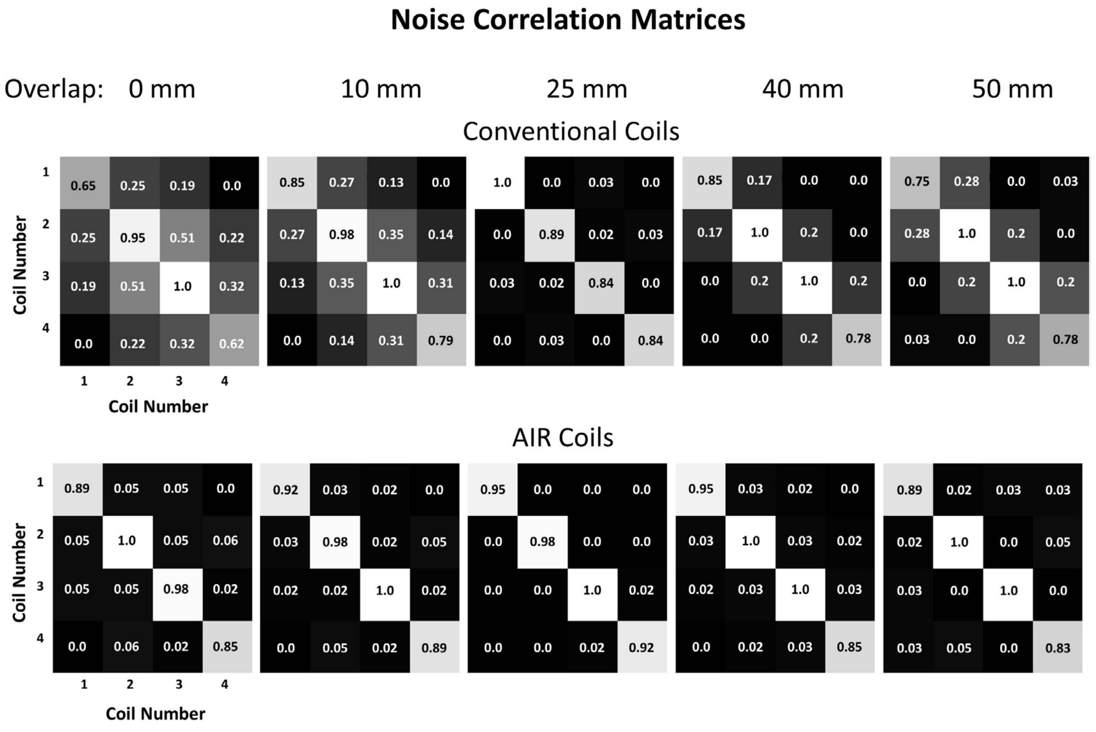

Figure 9. Noise correlation matrices for the linear four conventional (top row) and AIR coil (bottom row). The AIR coil shows lower correlation (off-diagonal values) compared to the conventional coil design, especially with non-optimal overlap.

distances of 0 mm, 24 mm and 30 mm was statistically significantly greater than the conventional coil combination at an overlap of 50 mm.

Figure 9 shows the noise correlation matrices for the four coil linear combination of the conventional (top row) and AIR coil (bottom row) RF coils. The diagonal elements of the matrix quantify the total noise power of a given element while the off-diagonal elements describe noise correlations between multiple elements (Ohliger and Sodickson 2006). For each matrix, the normalized correlation values are shown. These values were normalized to a maximum value of 1.0 by taking the absolute value, and then dividing individual correlation values by the largest value within the matrix. Given these characteristics, it is observed that the amount of correlated (off-diagonal) noise is less in the AIR coil elements compared to the conventional coil elements. The off-diagonal correlation values of the AIR coil matrix are consistently near zero for all overlaps indicating that the full SNR

Table 4. Average and standard deviation g-factor values as a function of coil overlap for both four coil AIR and conventional RF coil element combinations as a function of coil overlap distance. For both coil types a total of four coils were used.

	Conventional		AIR	
Overlap Distance (mm)	Average	Standard deviation	Average	Standard deviation
0	1.342	1.132	1.093	0.202
10	1.110	0.168	1.080	0.127
25	1.084	0.117	1.090	0.111
40	1.121	0.138	1.095	0.119
50	1.187	0.155	1.098	0.113

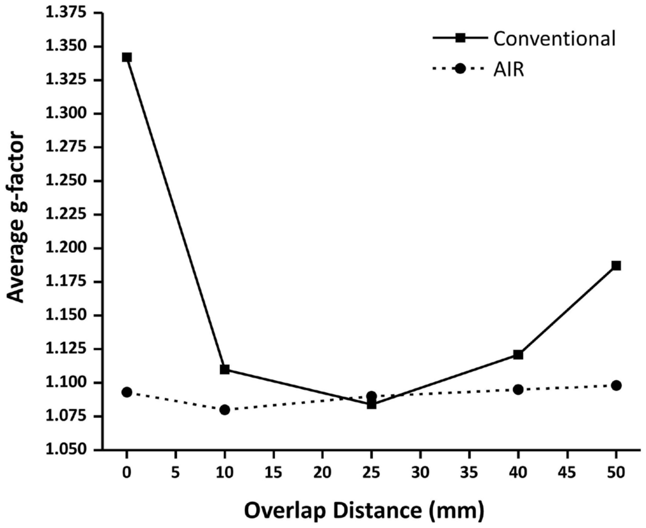

Figure 10. Average parallel imaging g-factors as a function of coil overlap distance for the four coil AIR and conventional coil combinations. AIR coils show relatively no change as a function of overlap distance compared to the conventional coil combinations which exhibit degradation in coil performance (increasing g-factor) away from the optimal overlap distance of 25 mm. Parallel imaging performance decreases with increasing g-value with a value of 1.0 representing optimal performance.

benefit of all coil elements is realized independent of overlap distance. At an overlap of 25 mm the conventional coil combination showed almost zero non diagonal elements indicating, again at the optimal overlap distance the SNR of the coil combination is maximized. However, as overlap distance deviates from the 25 mm value, non-diagonal values increase denoting coupling between coil elements. Overall, the AIR coil combination showed near-zero off-diagonal values for all overlaps, demonstrating an SNR advantage compared to conventional coils independent of overlap distance.

Table 4 lists both the average and standard deviation of the g-factor values acquired as a function of overlap distance for the AIR and conventional four coil combinations while figure 10 is a plot of the average values alone versus overlap distance for both coil types. As expected, at the optimal overlap distance of 25 mm, the coils exhibit similar performance characteristics with average g-factor values of 1.084 and 1.090 for the conventional and AIR coils respectively. At overlap distances less or greater than the optimal value for this coil diameter the parallel imaging performance of the conventional coil is degraded as seen by the increasing average g-factor value which degrades as overlap distance increases or decreases from the optimal. In contrast, the AIR coil exhibits almost no degradation in parallel imaging performance as a function of overlap distance with average g-factor values not exceeding a maximum of 1.1.

3.2. *In vivo* testing

Figure 11 shows axial images superior to the orbits at the level of the operculum obtained from the normal male volunteer scanned with the balaclava coil shown in figure 3. Despite the fact that the AIR coil is relatively loosely affixed to the balaclava—no more than four stiches per coil element and clear tape were used—the coils conform closely to the subject's anatomy and provide high quality MR images for both the T_1 FLAIR (figure 11(a)) and T_2 spin echo (figure 11(b)) acquisitions. Note that, as expected, there is signal drop off due to the absence of any coil elements covering the anterior anatomy. However, despite the lack of coil coverage, anterior anatomical structures including the right frontal gyrus (arrow) can be easily seen. Anatomical structures posterior to frontal gyrus are clearly visualized with the four coil combination and despite the variable overlaps between adjacent coil elements, the images display a high degree of image uniformity. It is important to note that no surface coil

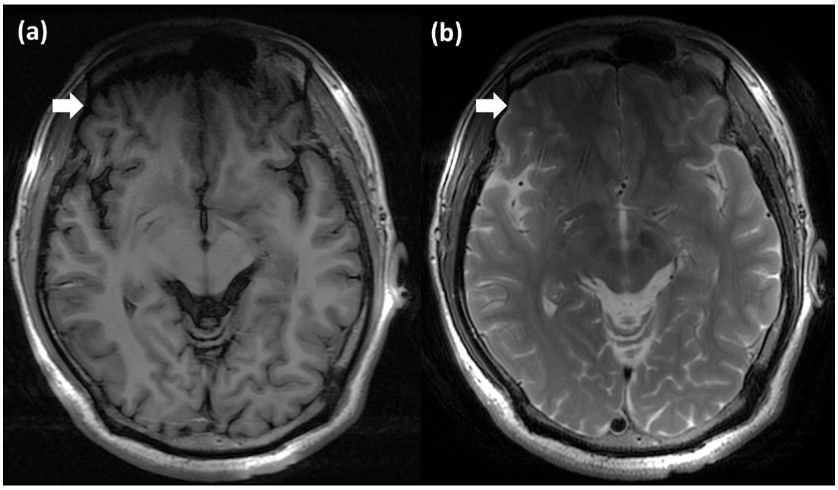

Figure 11. Axial T_1 FLAIR (a) and T_2 multi echo spin echo (b) images at the level of the operculum of the normal volunteer shown in figure 3. The arrow identifies the location of the right frontal gyrus.

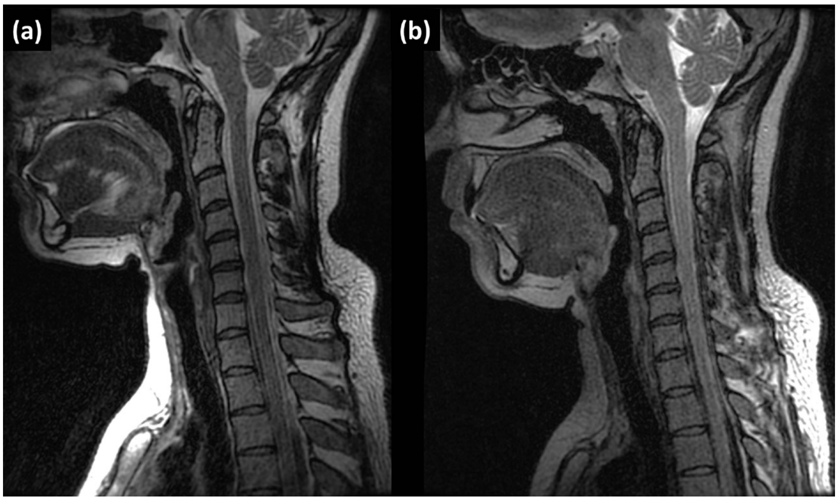

Figure 12. Coil comparison for MR imaging of RT patients. A single slice obtained from a non fat suppressed sagittal T_2-weighted, 3D multi echo spin echo of the normal female volunteer using the 16 element AIR coil (a) and 30 element FDA approved RT Suite coil configuration (b). Signal intensity variations across the imaging field of views are the result of individual coil placement around the volunteer.

intensity correction algorithms were applied to the images, and they represent the native images acquired from the 3.0 T MR scanner.

Figure 12 shows sagittal images of the cervical spine obtained from a normal female volunteer using both the 16 channel AIR coils (figure 12(a)) and 30 channel RT Suite (figure 12(b)). Both images are a single sagittal slice obtained from the 3D T_2-weighted multi echo spin echo sagittal acquisition described in table 1 (Experiment Number 4). Both images have equal window and level values and demonstrate that, despite having approximately half of the number of RF coil elements, the AIR coil design provided qualitatively similar image quality when compared to the 30 channel FDA approved coil. Signal intensity variations across the field of view of both data sets are the result of placement of individual coils within each coil set. Subtle differences in slice location between figures 12(a) and (b) are due to the physical repositioning of the subject that occurred when exchanging coil sets. However, as described in table 1, identical imaging parameters were used to acquire the data represented in these figures.

Figure 13 shows a single sagittal slice obtained from the 3D fat saturated T_1-weighted acquisition described in table 1 (Experiment Number 5). Cervical spine imaging was performed for the purpose of external beam irradiation treatment planning of metastatic lesions in the cervical spine arising from adenocarcinoma of the prostate in a 78 year old male. Figure 13(a) shows the result of using the 16 channel AIR coil while 13(b) shows that from the 30 channel FDA approved coil. The arrow identifies susceptibility induced artifacts arising from the placement of spine fixation hardware. Relative differences in signal intensity between the two image data sets across the imaging field of view are due to the placement of the individual RF coils.

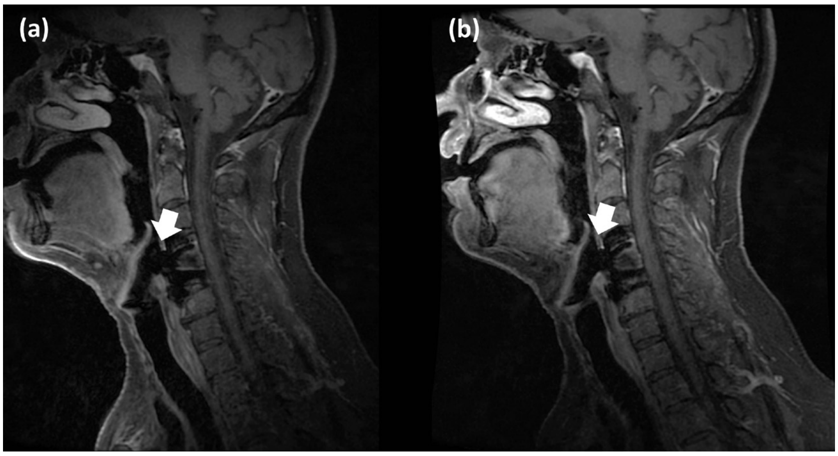

Figure 13. Coil comparison for MR imaging of RT patients. A single T_1-weighted, fat suppressed image obtained from a sagittal 3D multi echo spin echo acquisition of a patient undergoing MR imaging for RT treatment planning obtained using the 16 element AIR (a) and 30 element FDA approved RT Suite coil configuration (b). The arrow identifies signal loss and distortion due to the placement of spinal fixation hardware.

4. Discussion

Historically, the design and construction of multi-channel RF receive-only coils has been constrained by the need for a fixed physical geometry of individual coil elements, most notably the overlap amongst nearest neighbors (Roemer *et al* 1990). In addition, coil manufacturers have constructed either rigid or semi rigid housings to prevent damage and electrical breakdown of individual coil elements due to physical stress and distortion when placed around a patient. As a result, these coils have been ill-suited for RT treatment planning in which patients are imaged in non-neutral treatment positions which cannot be altered. The use of immobilization devices for RT treatments further complicates coil placement and can decrease image quality by requiring that coils be placed outside the device, further from the patient. The use of the linked resonator and interfacing electronics module combination (i.e. AIR coil) has the potential to address these limitations by relaxing the requirement on coil overlap distance, creating opportunities to increase or decrease coil density and allowing for overlap between adjacent coil arrays. The thin conductor construction of each coil element makes them flexible and durable while the miniaturization of the coil resonant circuitry decreases their overall form factor thereby facilitating fabrication of coils that can closely conform to the complex patient surfaces. Phantom and *in vivo* testing presented in this work provides quantitative evidence to support these claims.

Previously, Corea *et al* (2016, 2017) have described the use of screen printing techniques involving the deposition of conductive silver ink onto the opposite surface of a plastic substrate to create a flexible and thin RF coil elements. The sandwiching of the plastic substrate between the two conducting layers provides the capacitance necessary for tuning and matching circuitry while the thin nature of both the plastic and metal deposition create a low form factor and flexible RF coil. The AIR coil design reported in this work is fundamentally different from this approach for several reasons. First, the Corea design is electrically equivalent to the lumped circuit design used in existing RF coils as shown in figure 1(b). As such, the same limitations in terms of mutual inductance between coil elements exists thereby imposing the restriction on a predetermined coil overlap distance for multi element RF coils. Second, while screen printing of the circuit onto a thin plastic film provides a flexible substrate upon which to create and RF coil, the geometry of both individual coil loops and the overall coil remain unchanged. Unlike the balaclava coil shown in figure 3 in which the shape of individual coil elements can change based on the fitting of the fabric around an individual subject's head, the plastic substrate imposed a fixed geometry on the RF coil configuration. Finally, the increased decoupling between coil elements using the AIR coil technology creates opportunities to create extremely high coil density arrays that cannot be achieved with conventional coil designs, despite how thin or flexible these designs may be.

Vasanawala *et al* (2017) have reported on the development of a 16 element 'blanket' AIR coil for pediatric imaging applications. The 16 element blanket can be used on its own or in combination with posterior coil elements from FDA approved coils from the MR scanner manufacturer (GE Healthcare, Waukesha, WI) including the pediatric posterior array, posterior cardiac array and the posterior array from a standard adult torso coil. As in this work, the authors reported similar performance characteristics of the AIR coil design compared to conventional RF coils. The authors also noted that the decoupling between coil elements as seen in the noise correlation matrix for the 16 element coil remained effectively unchanged when flexed in two dimensions. For conventional coils in which a change in shape will result in a shift in resonant frequency of the coil (Mehmann *et al* 2017) and result in changes in coil coupling, no change in the noise correlation matrix indicates the robustness of these elements to shape distortion. Taken together, the work described in this report and that by Vasanawala *et al* (2017) demonstrate the utility of this new technology and the potential application beyond the sub specialty imaging application of MR for RT treatment planning and pediatric imaging.

This work provides both quantitative and qualitative data illustrating the superior performance characteristics of AIR coils when compared to equivalent conventional copper based designs. Normalized SNR maps for two coil combinations (figure 7) illustrate the relative insensitivity of coil overlap distance for AIR coils compared to conventional ones. This is particularly evident in the region of the overlap between coils in which conventional coil SNR maps show regions of signal loss (0 mm overlap) and significant heterogeneity (overlap distances of 30 mm and greater). In contrast, the overall SNR profile for AIR coils remains relatively constant as a function of coil overlap. Table 3 provides quantitative assessment of SNR data for the two coil combination and identifies that, based on SNR values alone, for overlap distances of 0 mm and 50 mm the AIR coil mean was statistically significantly greater that the conventional coil mean. However, at overlap distances close to the optimal overlap distance for the 110 mm coil diameter, the differences in SNR means were not statistically significant (24 mm and 30 mm overlap). This is somewhat expected as the effects of mutual inductance will be minimal at these overlap distances and therefore the SNR profiles should be similar as seen in figure 6(b). The relative insensitivity to coil overlap distance is graphically illustrated in the noise correlation matrices shown in figure 9 and further supports the fact that at the optimal overlap distance, the matrices for the four coil combination for both coil types are similar. However, at distances other than the optimal overlap distance, coil-to-coil interactions become evident for the conventional coil design. The overall superiority of the new coil design is also demonstrated in the *g*-factor data derived from the four coil phantom experiments as seen in figure 10 and table 4. While parallel imaging performance is dependent upon overlap distance for the conventional coil design, the AIR coil design demonstrates almost no dependence on overlap distance. Finally, *in vivo* testing in both normal volunteers and patient data demonstrate that these coils can conform closely to an individual's anatomy and provide images comparable to commercially available RF coils with larger numbers of coil elements.

There are several limitations related to this work. First, the electrical properties of both coil types were not fully characterized in this report. Parameters including overall coil quality (Q) factor, self-inductance (L) and resistance (R) are not reported. However, these values for a two element RF coil were previously reported (Vasanawala *et al* 2017). As such, the authors felt that it would be redundant to reproduce the same data that had been previously reported. Secondly, the *in vivo* comparison of the 16 element AIR coil and the FDA approved RT coil suite was not optimal due to the disparity in the number of coil elements between the two coil types. As noted previously, the commercial coil configuration included almost twice as many RF coil elements compared to the AIR coil with the expected decrease in overall image uniformity as seen in figures 12 and 13. However, despite the decreased element count, the AIR coil images produced images with image quality subjectively comparable to those produced with the commercial coil combination. To address this discrepancy, future work will involve the development of a 32 element AIR coil design using thinner and more flexible materials similar to those used in the balaclava coil.

5. Conclusion

In conclusion, this work has demonstrated that new, flexible AIR coils can be used for MR imaging of RT patients and that they provide advantages not seen with conventional RF coils.

ORCID iDs

Kiaran P McGee https://orcid.org/0000-0002-4750-5319

References

Brau A C S, Beatty P J, Skare S and Bammer R 2008 Comparison of reconstruction accuracy and efficiency among autocalibrating data-driven parallel imaging methods *Magn. Reson. Med.* **59** 382–95

Corea J R, Flynn A M, Lechêne B, Scott G, Reed G D, Shin P J, Lustig M and Arias A C 2016 Screen-printed flexible MRI receive coils *Nat. Commun.* **7** 10839

Corea J R, Lechene P B, Lustig M and Arias A C 2017 Materials and methods for higher performance screen-printed flexible MRI receive coils *Magn. Reson. Med.* **78** 775–83

Fujita H 2007 New horizons in MR technology: RF coil designs and trends *Magn. Reson. Med. Sci.* **6** 29–42

Haacke E M, Brown R W, Thompson M R and Venkatesan R 1999 *Magnetic Resonance Imaging: Physical Principals and Sequence Design* (New York: Wiley)

Kellman P and McVeigh E R 2005 Image reconstruction in SNR units: a general method for SNR measurement *Magn. Reson. Med.* **54** 1439–47

Mehmann A, Vogt C, Sporrer B, Varga M, Huang Q and Troester G 2017 *Int. Society of Magnetic Resonance in Medicine 25th Annual Meeting & Exhibition (Honolulu, HI, 2017)* p 764

National Electrical Manufacturers Association (NEMA) 2008 MS 9-2008 (R2014) characterization of phased array coils for diagnostic magnetic resonance images (MRI) Rosslyn, Virginia *Technical Report* p 24

Ohliger M A and Sodickson D K 2006 An introduction to coil array design for parallel MRI *NMR Biomed.* **19** 300–15

Pruessmann K P, Weiger M, Scheidegger M B and Boesiger P 1999 SENSE: sensitivity encoding for fast MRI *Magn. Reson. Med.* **42** 952–62

Reeder S B, Wen Z, Yu H, Pineda A R, Gold G E, Markl M and Pelc N J 2004 Multicoil Dixon chemical species separation with an iterative least-squares estimation method *Magn. Reson. Med.* **51** 35–45

Roemer P B, Edelstein W A, Hayes C E, Souza S P and Mueller O M 1990 The NMR phased array *Magn. Reson. Med.* **16** 192–225

Rossman P, Stormont R, Lindsay S, Robb F, Savitskij D, Stanley D, Huston J, Kaufmann T and McGee K P 2017 *Int. Society of Magnetic Resonance in Medicine 25th Annual Meeting & Exhibition (Honolulu, HI, 2017)* p 763

Skinner T E and Glover G H 1997 An extended two-point dixon algorithm for calculating separate water, fat, and B0 images *Magn. Reson. Med.* **37** 628–30

Sutherland J 1999 As edge speeds increase, wires become transmission lines *EDN Network* (https://m.eet.com/media/1140649/19791-85208.pdf) pp 75–94

Vasanawala S S *et al* 2017 Development and clinical implementation of next generation very light weight and extremely flexible receiver arrays for pediatric MRI (New York: Cornell University Library) (arXiv:1705.00224)

Veenstra H and Long J R 2008 *Circuit and Interconnect Design for RF and High Bit-rate Applications* vol 1 (Berlin: Springer)